Role of Bi-excess on structural, electrical, optical, and magnetic properties BiFeO$_3$ nanoparticles

Anju Kumari[1], Kavita Kumari[2], Faheem Ahmed[3], Mohamad M. Ahmad[3], Jyotsna Sharma[1], Ankush Vij[4,*], and Shalendra Kumar[3,4,*] (ORCID)

[1] Electronic Materials & Nanomagnetism Lab, Department of Applied Physics, Amity School of Applied Sciences, Amity University Haryana, Gurgaon 122413, India

[2] School of Materials Science and Engineering, Changwon National University, Changwon, Gyeongnam 51140, Republic of Korea

[3] Department of Physics, College of Science, King Faisal University, Hofuf, P.O Box 400, Al-Ahsa 31982, Saudi Arabia

[4] Department of Physics, University of Petroleum & Energy Studies, Dehradun 248007, India

ABSTRACT

The influence of Bi content on structural, optical, and multiferroic properties of BiFeO$_3$ has been studied. The nanoparticles of BiFeO$_3$ with different Bi content such as Bi$_{0.00}$FeO$_3$, Bi$_{0.03}$FeO$_3$, Bi$_{0.05}$FeO$_3$, Bi$_{0.07}$FeO$_3$, and Bi$_{0.10}$FeO$_3$ have been prepared using the nitric acid-assisted sol–gel method. The structural analysis of XRD patterns via Rietveld refinement revealed rhombohedral structure with $R3c$ phase along with the minor secondary phase of Bi$_2$Fe$_4$O$_9$. The crystallite size calculated using Scherrer's formula was found to be in the range 56 nm $\sim$ 41 nm. The lattice parameters and density were found in the range 8.78–8.81 Å and 6.10–6.13 g/cm^3, respectively. The highest value of maximum polarization and remnant polarization were found to be 1.15 μC/cm^2 and 0.90 μC/cm^2, respectively, for Bi$_{0.05}$FeO$_3$ nanoparticles. The Bi$_{0.05}$FeO$_3$ nanoparticles also showed a high dielectric constant with a smaller dielectric loss. The grain and grain boundaries have shown excellent electrical behavior as investigated via impedance, Modulus, and ac conductivity. The UV–Vis spectroscopy demonstrated that the Bi$_{0.05}$FeO$_3$ nanoparticles show the maximum bandgap of $\sim$ 1.96 eV. The dc magnetization results infer the weak ferromagnetic behavior of the Bi-excess—BiFeO$_3$ nanoparticles and indicate a maximum saturation magnetization of 0.24 emu/g for Bi$_{0.05}$FeO$_3$ nanoparticles.

1 Introduction

Micro-scale multiferroics, which are of outstanding fundamental and technological interest, show a vital order of electrical, optical, and magnetic property as a result of their minimum dimension and size effects [1–3]. Since 1959, the multiferroics have demonstrated a theoretical possibility of coupling electric and magnetic degrees of freedom in a single material. In the last few decades, BiFeO$_3$ (BFO) has gained

Address correspondence to E-mail: ankush82@gmail.com; shailuphy@gmail.com

significance due to the possibility of controlling the magnetoelectric coupling in a single device. BFO relates to the rhombohedral perovskite family with *R3c* space group which connotes multifunctional features of ferroelectricity and ferromagnetism together at room temperature [4]. It possesses twisted perovskite pseudocubic and hexagonal structures that have an inbuilt distortion due to spin structures that suppress the supervision of linear magnetic effects [5, 6]. It has ferroelectric Curie temperature (T_C = 1100 K) and G-type antiferromagnetic ordering with Néel temperature (T_N = 653 K). The multiferroic and electrical properties of BFO are extremely sensitive to defects such as secondary phases, vacancies, and interstitials [2]. Though these defects are insignificant and detrimental in bulk, they have a profound influence in altering the properties at the nanoscale because of the large surface area. In literature, the defects such as oxygen vacancies have been reported to be the main reasons for anomalous electronic properties in oxide nanoparticles (NPs) [7].

Thereby, as regard the functional properties, low-dimensional BFO has shown dramatic difference as compared to bulk and thin films. For example, the magnetization of BFO can be enhanced by uncompensated spins at the surface induced by NPs due to the large surface-to-volume ratio [2, 8, 9]. This evolution made BFO as one class of the most promising multiferroic materials [9, 10]. However, the multiferroic orders have been quite difficult to achieve because of the large leakage currents that arise from defects such as secondary phases and oxygen vacancies. Therefore, the efficiency of BFO is affected by non-stoichiometry and leakage currents caused by the impurities [9]. In multifunctional devices, multiferroic materials have the coexistence of a minimum of two switchable states, i.e., polarization and magnetization, which assure a vital order of uses. Single-phase BFO has more potential as a multiferroic material because magnetoelectric coupling occurs at room temperature. The impurities, observed as the secondary phases, elongate into three different regions: first is the evaporation of the bismuth element in an increasingly easy way of synthesis due to the decreased temperature of the dissolved Bi-salt with the formation of Bi_2O_3. Second, the synthesis of single-phase BFO coexisting with two secondary phases ($Bi_2Fe_4O_9$ and $Bi_{25}FeO_{39}$) [11, 12]. The third is the change in the chemical valence state of Fe ions in an oxygen-deficient atmosphere. This charge defect

with respect to the Fe^{2+} ion developed in the synthesis is usually referred to as the maximum leakage current of BFO [1, 8].

In addition to the multiferroic properties, BFO also exhibits exceptional optical properties that add to its functional utilization. Multiferroics are able to change light into electrical, mechanical, and chemical energies. The main interest of studying optical properties of multiferroic materials is their practical applications in transducers, spintronics, ferromagnetic resonance devices, quantum electro-magnets, microelectronic devices, etc. Alongside being ferroelectric, BFO exhibits an intrinsic spontaneous polarization at the core of the photoinduced phenomenon. So that, once the light excitations generate electron–hole pair, the polarizations act as an internal electric field favoring the charge carrier separation and thus repressing their recombination [13]. For photoinduced applications, among useful ferroelectrics, the BFO-based materials are the proving candidate because of their comparatively smaller bandgaps ($\sim$ 1.7–2.0 eV) as compared to other definitive ferroelectric oxides like $BaTiO_3$, $LiNbO_3$, and $PbZrTiO_3$ (E_g > 3.1 eV), which permits the profit from a wide portion of the electromagnetic spectrum. In addition, the large polarizations also assure greater efficiency for separations of the charge carriers [8]. For instance, spontaneous polarization of 30 and 44$\mu C/cm^2$ have been reported in BFO NPs and ceramics, respectively [6]. However, other reports on BFO ceramics showed small electric polarization and non-saturated hysteresis loops [6, 8, 13], which were assigned to electrical leakage current. Likewise, the ferromagnetism in multiferroics has also been found to be influenced by the structure, morphology, and variation in the bandgap. It has been observed that changes in particle size and morphology have a substantial effect on the optical properties such that the change in particle size in between nano and micrometer scale has been found to cause the bandgap variation up to 1.81–2.20 eV [13].

Furthermore, various methods have been utilized to form the single phase of BFO like sol–gel, rapid liquid sintering, co-precipitation, and mechanical activation [6, 11, 12, 14]. Out of these, the sol–gel process is one such method that can be performed at low synthesis temperatures (301–550 °C) and reduces secondary phases to a great extent. Utilizing oxygen-enriched atmospheres could hold these Fe ions in Fe^{3+} form, which minimizes the leakage currents of

BFO. The main cause behind the maximum leakage current is assigned to the oxygen vacancies and minimum content of Fe^{2+} ion in perovskite material. Therefore, in the present work, the sol–gel method has been used to synthesize NPs of BFO with Bi-excess. To enhance ferroelectric and ferromagnetic orders and to reduce the leakage current problem, the optimization of structural, multiferroic, and optical properties of synthesized NPs have been carried by investigating through X-ray diffraction (XRD) analysis, P–E loop measurements, dielectric constant, loss tangent (tan δ), ac conductivity (σ_{AC}), modulus spectra analysis, impedance analysis, Cole–Cole analysis of the impedance, UV–vis analysis, and magnetization.

2 Experimental details

2.1 Materials and methods

For the synthesis of bismuth ferrites ($Bi_{1+x}FeO_3$) ($x = 0.00, 0.03, 0.05, 0.07$, and 0.10) NPs, sol–gel process was used. The bismuth nitrate pentahydrate [Bi $(NO_3)_3 \cdot 5H_2O$] (AR, 98.5%) and iron nitrate nonahydrate [Fe $(NO_3)_3 \cdot 9H_2O$] (AR, 99.5%) were weighed properly to make a solution of 0.1 M. The following procedure has been used for the synthesis:

In double distilled water, citric acid ($C_6H_8O_7$) was used as a solvent, and the ratio of metal nitrate and citric acid was kept 1:1. Afterward, Bi $(NO_3)_3 \cdot 5H_2O$ was added to the solvent, and some extent of concentrated nitric acid (HNO_3) was used to dissolve it. Later on, Fe $(NO_3)_3 \cdot 9H_2O$ was added to the above solution to get the compound in the proper ratio. Finally, ethylene glycol was added to the mixture along with stirring at 90 °C for the formation of a gel. Then, the light yellow-colored solution was obtained under vigorous stirring. The obtained powder was calcined at 550 °C for 2 h to get well-crystallized BFO NPs, as shown by the schematic in Fig. 1. Finally, the samples were ground to fine NPs, pressed into circular pellets by applying a pressure of 5 tons, and then sintered at 600 °C for 2 h. The thickness of the pellets was maintained at $\sim$ 1–1.5 mm. The surfaces of the pallets were polished and coated with silver paste in order to make them act as good electrodes for measuring the dielectric properties. The nanoparticles of $BiFeO_3$ with different Bi content such as $Bi_{0.00}FeO_3$, $Bi_{0.03}FeO_3$, $Bi_{0.05}FeO_3$, $Bi_{0.07}FeO_3$, and $Bi_{0.10}FeO_3$ nanoparticles were referred to as BFO, BFO3, BFO5, BFO7, and BFO10, respectively.

2.2 Sample characterizations

The samples were characterized using x-ray diffraction (XRD) in the range of 15–90°, with $\lambda = 0.15406$ nm. The FE-SEM measurements were performed at Merlin Compact. The P–E loops were traced using P–E Loop Tracer with an internal capacitance of 100 nF and an internal resistor of 100 K with a Triangular wave. The maximum field of 5 kV/cm was applied on the samples, measured MARINE PE—01 P–E Loop Tracer System. The dielectric properties have conveyed out using Alpha-A High-Performance Frequency Analyzer at room temperature in the frequency range from 1.0 Hz to 10 MHz. To register the UV–Visible optical spectra, S-4100 (SINCO Instrument Co.) photospectrometers were used in the wavelength order of 400–800 nm at room temperature. The magnetization measurements were carried at the VSM module of the cryogen-free physical property measurement system (PPMS), VersaLab developed by Quantum Design.
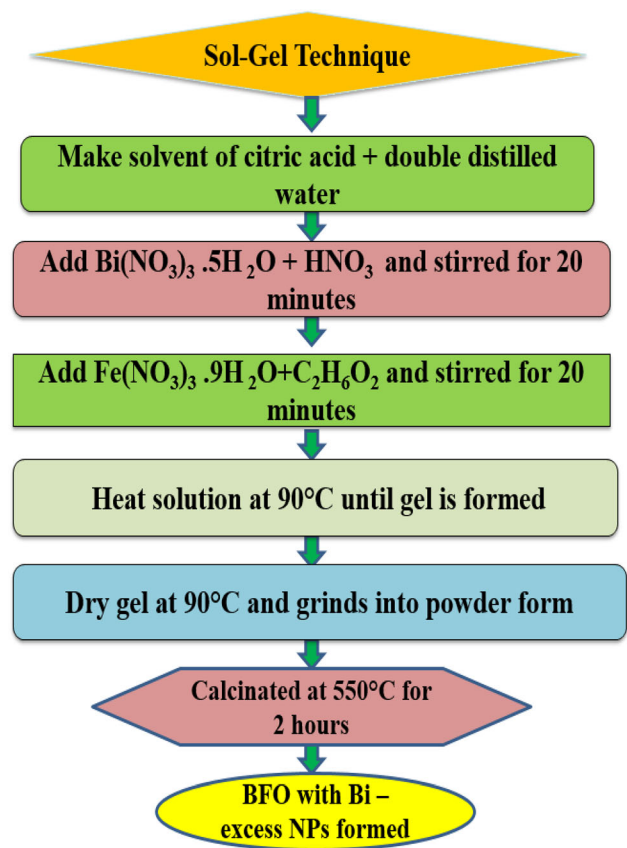

Fig. 1 Flowchart of the synthesis process of Bi-excess BFO NPs

3 Results and discussion

3.1 X-ray diffraction analysis

The X-ray diffraction (XRD) patterns of BFO, BFO3, BFO5, BFO7, and BFO10 NPs are shown in Fig. 2a, b. All the samples have been characterized with rhombohedral perovskite crystal structure. The peaks show well crystallization of the samples, which have been prepared by the sol–gel method. The Rietveld refinement of XRD patterns of all the samples is shown in Fig. 2a. The black, red, blue, and pink lines represent the experimental, theoretically fitted curve; the difference between the experimental and theoretical measurements; and the 2θ positions of the Bragg's reflections, respectively. The peak positions show an apparent splitting along with the reduced intensity and indicate a rhombohedral picture with the $R3c$ space group having unit cell parameters of $a = b = c$ and $\alpha = \beta = \gamma \neq 90$. The (104) and (110) peaks are most intense in comparison with other peaks, as displayed in Fig. 2b. The indexing of the XRD peaks reveals the rhombohedral lattice symmetry, which is in agreement with the reported results in the literature [15]. The peak shifting towards lower 2θ value for BFO5 and towards higher 2θ values has been observed for other samples as compared to pure BFO which is indicative of the change in the lattice parameter. The lattice parameters for all the samples have been shown in Table 1 as determined from the Rietveld refinement. It is

observed that the minimum value of lattice parameters has been obtained for BFO5 nanoparticles which may be associated to the different ionic state of metal ions. It is noteworthy to mention here that in BFO5 nanoparticles, excess of Bi_2O_3 during the synthesis may compensate the deficiency of Bi ion the sample, which generally happens because of its (Bi) volatile nature, therefore, in this situation most of the Fe ions remain in $+3$ valence state. This may be the reason, we have obtained the lowest value of lattice parameter and unit cell volume in the case of BFO5 sample. The increase in the lattice parameters in other composition may be due to the formation of defects such as iron, oxygen, and bismuth vacancies as well as mixed balance state of Fe^{2+} and Fe^{3+} ions. Furthermore, the values of the reliability factors obtained from the Rietveld refinement have been listed in Table 2. In addition, the extra peaks at about 27° are also marked as secondary peaks that may be associated with $Bi_2Fe_4O_9$ as per the literature, which usually appears in the range of 25° and 30° [15]. These peaks can be ascertained only when the X-ray observations are conveyed out with higher intensity sources. In the present case, the fraction of the secondary peak has been found to be maximum for BFO10 NPs having 2.05%. However, this percentage is small at lower Bi content, being most insufficient for BFO5 (0.52%). The secondary peaks can be assured to the volatilizations of Bi^{3+} ions which result due to the extra addition of bismuth. The higher

Fig. 2 **a** Rietveld refinement of XRD patterns of all compounds of BFO, BFO5, BFO7, and BFO10. The peaks of impurity phase ($Bi_2Fe_4O_9$) are marked with *; **b** The enlarged image of the highest intensity peak for all the samples
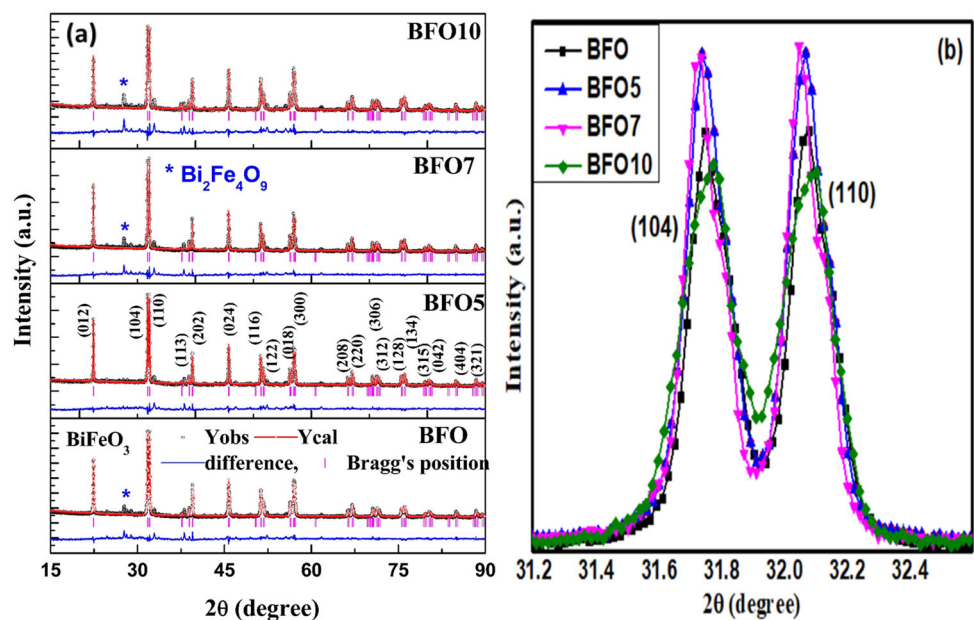
Table 1 Structural parameters obtained from Rietveld refinement of XRD patterns

Composition	Particle size (nm)	Lattice Parameter (Å)	Strain ($\times\ 10^{-3}$)	Density (g/cm^3)	Cell volume (Å^3)	Dislocation density (δ) ($\times\ 10^{-4}$)
BFO	47	8.80	2.7	6.10	681.35	4.5
BFO5	41	8.78	3.1	6.13	677.53	5.9
BFO7	56	8.79	2.2	6.12	677.94	3.1
BFO10	52	8.81	2.4	6.09	682.63	3.6

Table 2 The values of the reliability factors obtained using the Rietveld refinement

Composition	R_{p} (%)	R_{wp} (%)	R_{exp} (%)	χ^2
BFO	20.2	19.3	9.37	4.2
BFO5	20.2	19.2	8.75	4.8
BFO7	18.5	17.8	8.79	4.1
BFO10	23.4	22.4	9.17	5.9

vapor pressure of bismuth tends to quickly evaporate the Bi^{3+} ions during synthesis, such as drying and annealing conditions in bismuth excess series of BFO. Further, the particle size has been calculated using Scherrer's equation [16]:

$$\text{Particle size }(D) = \frac{K\lambda}{\beta \text{Cos}\theta} \qquad (1)$$

where D = average crystallite size; K = 0.89, the shape factor; λ = 0.15406 nm, wavelength of using the samples; β = FWHM; 2θ = Bragg's angle. The particle size has been found to be minimum (41 nm) for BFO5 NPs with the least lattice parameter of 8.78 Å exhibiting enhancement with the Bi-excess. In addition, the strain has been calculated using the formula: $\beta = 4\ \varepsilon\ tan\theta$ and observed to be minimum for the smallest size NPs (BFO5). The dislocation density has been calculated using the following formula [15]:

$$\text{Dislocation density }(\delta) = \frac{1}{D^2} \qquad (2)$$

The obtained values of the structural parameters for all the samples are displayed in Table 1.

3.2 Morphological properties

The field emission electron microscopy was used to study the surface morphology of Bi-excess $BiFeO_2$ nanoparticles. The morphological analysis of BFO, BFO3, BFO5, BFO7, and BFO10 NPs is presented in

Fig. 3a–e. The micrographs display a broad distribution of the particle sizes. The particles exhibit spherical shape morphology, which persists for all the samples. It is clear from the FE-SEM micrographs that all Bi-excess nanoparticles are composed of nanocrystalline grains. The histograms of the particle size distribution have been attached with the respective micrographs. The particle sizes obtained after the fitting of the histograms are in agreement with the outcomes obtained from XRD analysis, providing minimum particle size for BFO5.

3.3 Ferroelectric properties

In multiferroics, the ferroelectric orders are formed as a result of the irreversibility of the polarizability by applied electric fields. The observance of the hysteresis has elements for the research on ferroelectrics. Figure 4a–e exhibits the ferroelectric hysteresis loops of BFO, BFO3, BFO5, BFO7, and BFO10 NPs at a frequency of 50 Hz at room temperature. Figure 4f shows a combined P–E hysteresis loop of all the samples for the sake of comparison. These loops indicate the favorable ferroelectric behavior of BFO NPs. It is observed that as Bi content increases, the loops look like standard ferroelectric curves. This may be associated with the reduction of leakage current, which may also have occurred due to the enhanced density of the defect states as a consequence of the formation of the vacancies. It is worth mentioning that perfect saturated ferroelectric curves in pure BFO are hard to obtain due to the high coercive fields and high leakage currents. The cause of leakage currents can be associated with the oxygen vacancy and Fe^{2+} in the form of impurity phases in the samples. [15]. The values of the parameters obtained from the analysis of the P–E hysteresis loops: maximum polarization (P_{max}), remnant polarization (P_r), and coercive electric fields (Ec) have been displayed in Table 3. It is found that the value of P_{max} increases upto BFO5 and then

Fig. 3 FE-SEM images of **a** BFO; **b** BFO3; **c** BFO5; **d** BFO7; and **e** BFO10
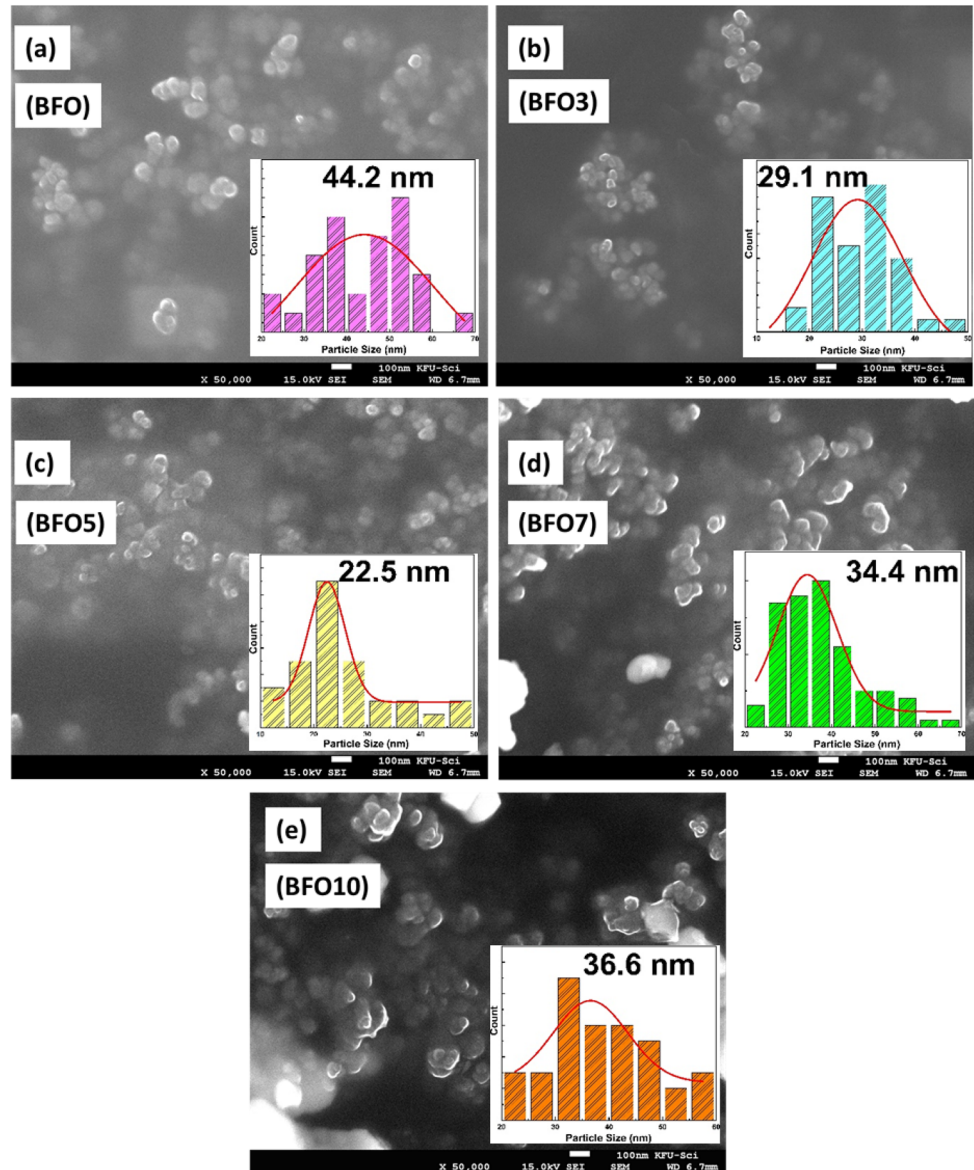
decreases. This infers that the increase in Bi content in the sample may lead to the increase in the electron density, which contributes to the more number of electric dipole moments per unit volume. Then increasing Bi-excess also increases the oxygen vacancies in the material. However, when the Bi content is increased beyond 5%, it may start to suppress the polarization. Therefore, the values of all the parameters have been found to be maximum for BFO5. Thus, the enhanced value of P_{max} for BFO5 shows that with the Bi-excess, the ferroelectric behavior of the NPs improves, which means Bi-excess in the NPs amplifies the polarization of the material and improve the ferroelectric properties of the material.

3.4 Electrical properties

3.4.1 Dielectric properties

Figure 4 shows the changes of real (ε') as well as imaginary (ε'') dielectric constant, and dielectric loss (tan δ) with frequency in BFO, BFO3, BFO5, BFO7, and BFO10. The dielectric constant (ε') in all the samples gradually decreases with increasing frequency (Fig. 5a) and becomes nearly frequency-independent beyond 100 kHz. The frequency dependence of the dielectric constant has been in agreement with the orientational relaxation of dipole and conduction of charge carriers. When the frequency increases, the dipoles are not able to vary
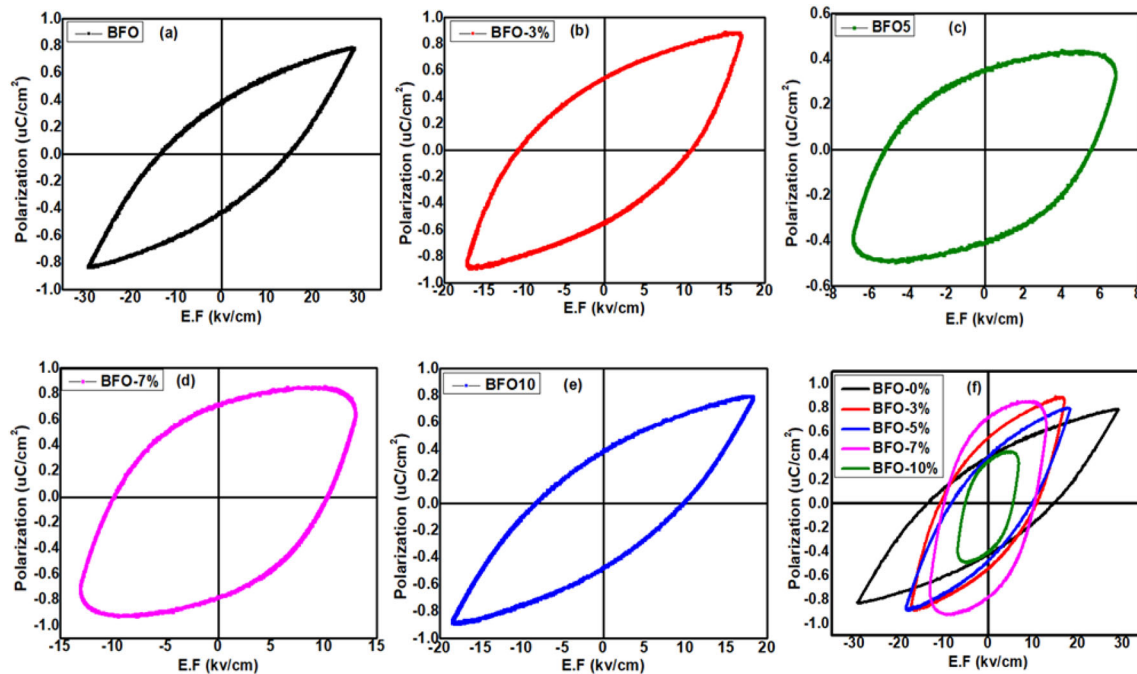
Fig. 4 The P–E hysteresis loops of the **a** BFO; **b** BFO3; **c** BFO5; **d** BFO7; **e** BFO10; and **f** Combined plots at 50 Hz frequency at room temperature

Table 3 The values of ferroelectric, dielectric parameters, and bandgaps

Composition	P_{max} ($\mu C/cm^2$)	P_r ($\mu C/cm^2$)	E_c (kV/cm)	α	Bandgap (eV)
BFO	0.58	0.21	34.28	0.83	1.72
BFO3	0.37	0.25	10.28	0.75	1.86
BFO5	1.15	0.90	14.82	0.90	1.96
BFO7	1.11	0.82	14.50	0.89	1.92
BFO10	0.35	0.31	15.38	0.87	1.89

their orientation with a rapidly oscillating electric field, causing ε' to decrease. At the minimum frequency of 100 kHz, the BFO exhibits a dielectric constant (ε') of 120 which increases to 210 for BFO5. After that, it decreases to 180 and 190 for BFO7 and BFO10, respectively. However, BFO3 NPs exhibit the lowest value of ε' at 80. Bi-excess NPs also show great sensitivity to frequencies. On the far side, towards 1 MHz, Bi-excess BFO NPs show lower values of the ε' as compared to the pure BFO NPs. Observations suggest that the dielectric constant is highly sensitive to the Bi content in BFO NPs [17]. The values of the dielectric constant (ε') of these samples can be calculated using the formula

$$\varepsilon' = C \times t/\varepsilon_0 \cdot A \tag{3}$$

where C is the capacitance of the specimen, t is the sample thickness, ε_0 is the permittivity in a vacuum equal to 8.854×10^{-12} C^2N^{-1} m^{-2}, and A is the area of the specimen in square meter. Moreover, at lower frequencies, the greater slope of pure BFO has been shown by plotting the ε'' with frequency (Fig. 5b). The decrease in ε'' is a consequence of reducing inner stress in the grain boundary. The grain boundary effect can be neglected for single crystal NPs, whereas, for the NPs having secondary phases, this effect cannot be neglected. Such a type of dielectric behavior clearly demonstrates the dependency on the grain size distribution and space-charge polarization [18]. The tan δ *vs* frequency curves are shown in Fig. 5c for all the samples. The pure BFO NPs show a dielectric loss peak at 1 Hz with tan δ of 2.5, and for Bi-excess BFO NPs i.e., BFO3, BFO5, BFO7, and BFO10; the dielectric loss decreases. In the low-frequency area, the tan δ has been attributed to the interfacial or space-charge distribution. At this stage, some extra contributions would come from grain boundaries and defect sites which act as a hindrance to the movement of charge carriers due to localized polarizations. In lower frequency regions, it is noticeable that conductivity rising due to oxygen
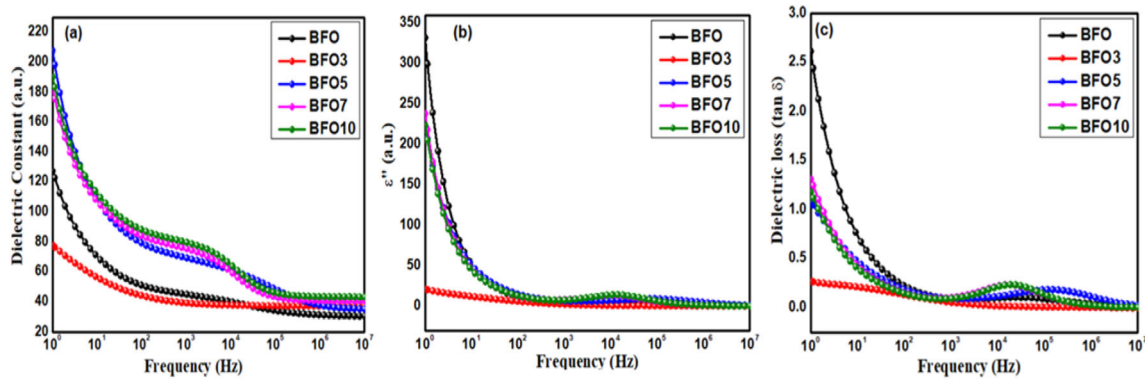
Fig. 5 Frequency dependence of **a** Real dielectric constant, **b** imaginary dielectric constant, and **c** Dielectric loss (tan δ) at room temperature

vacancies could be attributed to the dielectric dispersions. The oxygen vacancies are inherently produced in pure BFO NPs due to the volatile nature of the Bi atom. Although, it has been reported that a large number of oxygen vacancies are created when higher temperatures (750–850 °C) are employed for sintering NPs [19]. Nonetheless, for the present work, the samples were sintered at a minimum temperature of 550 °C expecting the minimum number of vacancies which leads to the high value of the dielectric constant and lesser value of the dielectric loss. Besides, a hunch can be observed at around 1000 Hz frequency in samples with high Bi content. Such type of feature points towards the presence of more than one type of relaxation phenomenon. It is possible that in addition to the relaxation due to interfacial charge distribution, the interior of the grains also undergoes dielectric relaxation. The additional dielectric relaxation in the interior of the grains may be associated with the enhanced density of states due to increased Bi content. It is worthy to recall here that this is the same reason responsible for the reduced polarization of the samples at higher Bi content.

Further, to examine the dielectric dispersions exhibiting the frequency-dependent dynamics of the NPs, the fitting of dielectric constants has been performed with the help of the Havriliak–Negami Model, as shown in Fig. 6a–e. The Havriliak–Negami model, introduced by A.S. Volkov et al. [20], has been successfully employed in the present case to investigate the behavior of dielectric constant in the samples. The width of the loss peak and the relaxation times are determined from the temperature-independent (α) and temperature-dependent (τ) parameters, respectively. The values of these parameters

obtained for all the samples are shown in Table 2. It is evident from the table that the value of α is closer to 1 in all the samples, which means that the dielectric relaxation is closer to the Debye relaxation [21].

3.4.2 AC conductivity

The ac conductivity (σ_{AC}) has been calculated using dielectric constant (ε') and dielectric loss (tan δ), as highlighted in Fig. 7 for all Bi-excess BFO NPs. It was measured by using the relation

$$\sigma_{AC} = \varepsilon\prime\varepsilon_0\omega \tan \delta \qquad (4)$$

where $\omega = 2\pi f$, $\pi = 3.14$, f = frequency, ε' is the dielectric constant, ε_0 is the permittivity of vacuum, and tan δ is the loss tangent. The ac conductivities in dielectrics are primarily because of the hopping of electrons between $Fe^{2+} \leftrightarrow Fe^{3+}$ ions of similar nature present in more than a single valence state. The electrical conduction mechanism in the samples can be explained using the electron hopping model employed by Kumar et al. [22]. The increase in linear variation at 1 Hz frequency shows that this frequency is sufficient to instigate the hopping conductivity. The ac conductivity is observed to increase acutely at lower frequencies and tardily at high frequencies with a higher slope for BFO5, BFO7, and BFO10. The BFO and BFO3 NPs exhibit comparatively smaller slopes. In addition to that, throughout the frequency range, the patterns exhibit some specific features like dispersions with changing slopes. Such features arise due to the interfacial polarization that can be explained on the basis of Koop's phenomenological theory [23]. These features are prominent in higher Bi-excess (BFO7, BFO10) NPs. Thus, the BFO5 NPs
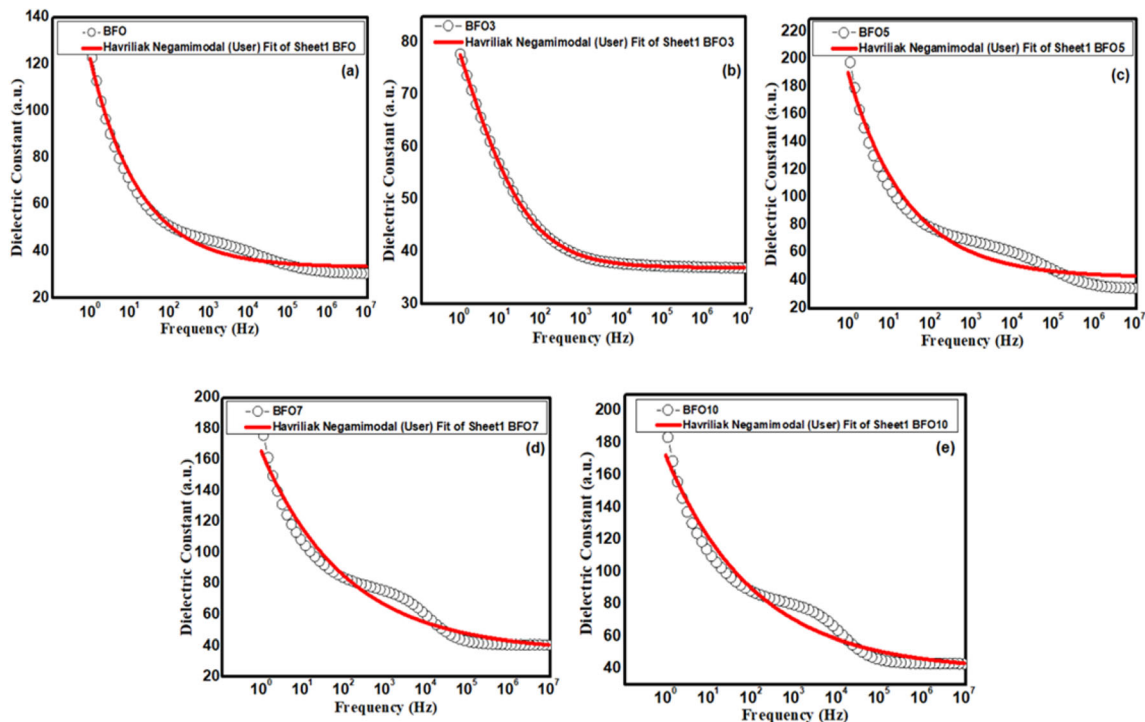
Fig. 6 Fitting of dielectric constant for **a** BFO; **b** BFO3; **c** BFO5; **d** BFO7; **e** BFO10 NPs with Havriliak–Negami model
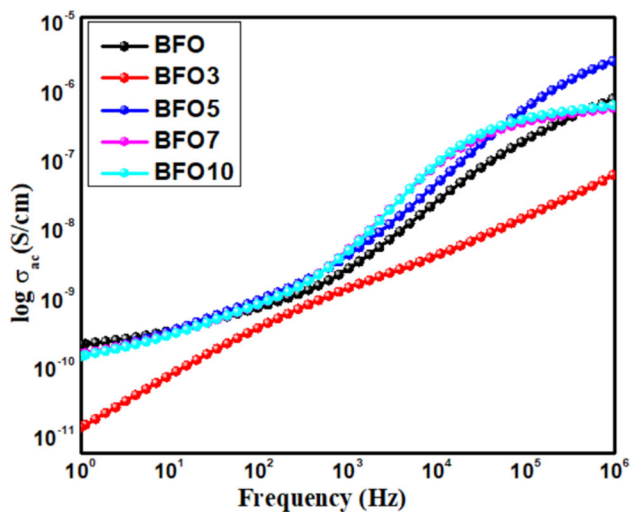

Fig. 7 Frequency-dependent ac conductivity plot for **a** BFO; **b** BFO3; **c** BFO5; **d** BFO7; **e** BFO10 NPs at room temperature

demonstrate a maximal correlation of the ac conductivity with the frequency among all the samples.

### 3.4.3 Modulus spectra analysis

The change of real (M') and imaginary (M'') parts of the electric Modulus as a function of frequency at room temperature are represented in Fig. 8a, b. The

increase in frequency, M' also increases which indicates towards the conduction processes of small range mobility of charge carriers. In addition, the values of M' also increase with Bi-excess BFO concentrations. Further, M'', indicating the energy loss in the NPs, demonstrates well-distinguished peaks in the range ~ 1 Hz–10 MHz. The low-frequency peaks show that ions can move over long distances by hopping from one site to the neighboring site. In contrast, a high-frequency peak indicates that ions can perform only localized motion with their confinement in potential well [18]. However, the asymmetric peaks towards the higher frequency indicate the correlation between mobile charge carriers from long- to short-range motilities giving rise to dissimilar time constants [24].

3.4.4 Impedance analysis

Impedance spectroscopy technique has been utilized to investigate the intra- and inter-granular contributions to the impedance in the studied compositions as a function of frequency to identify the electrical properties of BFO, BFO3, BFO5, BFO7, and BFO10 NPs. The contribution of the grain and grain boundaries to the electrical properties of the

Fig. 8 Frequency-dependent **a** real modulus; and **b** imaginary modulus of **a** BFO; **b** BFO3; **c** BFO5; **d** BFO7; **e** BFO10 NPs at room temperature
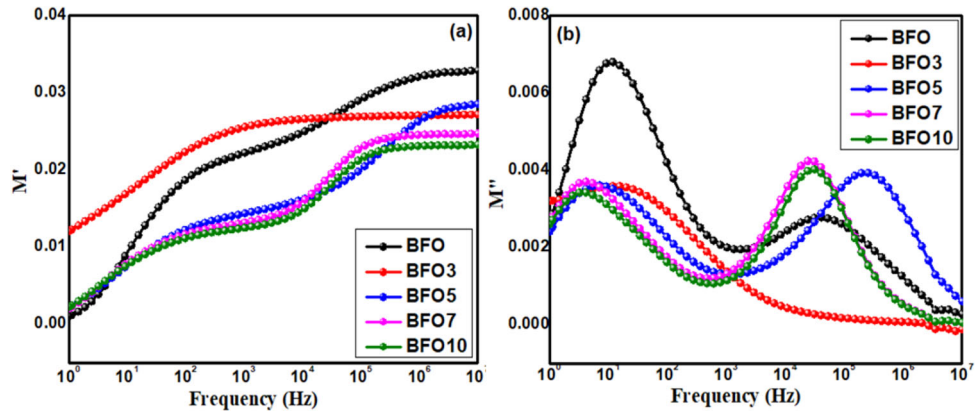
dielectrics can be understood via measuring impedance, etc. The information about internal conduction transport can be determined by measuring the complex impedance (Z^*) using the [25, 26]:

$$Z* = Z' + jZ,$$

where Z' is real part and Z'' is imaginary part of impedance. They are as given below:

$$Z' = R_g / \left(1 + \left(\omega_g C_g R_g\right)^2\right) + R_{gb} / \left(1 + \left(\omega_{gb} C_{gb} R_{gb}\right)^2\right)$$

where R_g is grain and R_{gb} is grain boundary resistance, similarly C_g is grain capacitance and C_{gb} is grain boundary capacitance. And ω_g and ω_{gb} are the frequencies. Due to grain and grain boundary, the capacitance and the relaxation time have been found using the following relations:

$$C_g = 1/R_g\omega_g$$

$$C_{gb} = 1/R_{gb}\omega_{gb}$$

$$\tau_{gb} = 1/\omega_{gb} = R_{gb}C_{gb}$$

$$\tau_g = 1/\omega_g = R_g C_g$$

Figure 9a, b shows the variation of real impedance (Z') and imaginary impedance (Z'') with frequency for the Bi-excess BFO NPs. The magnitudes of Z' have been observed to decrease linearly with frequency up to ~ 10 Hz. The plateau observed at frequency > 1 kHz expressed the possible exit of space-charge accompaniment with the diminution in resistant property of the material [27]. In addition, the value of Z' is also observed to be lower for BFO3, BFO5, BFO7, and BFO10 than that of BFO, which is in accordance with the dielectric constant. As observed from Fig. 9a, Z' has higher values in the low-frequency region, and it decreases monotonically with an increase in frequency and remains invariant at higher frequencies irrespective of temperature. Figure 9b shows the change of Z'' with frequency in the range (10^{-1} Hz–100 MHz). All the curves superimpose except that of BFO5. A clear peak shift towards higher frequency has been observed in the case of BFO5, which indicates the relaxation phenomena occurring in the material [28].

3.4.5 Cole–Cole analysis

The real impedance (Z') and imaginary impedance (Z'') are further used to calculate the effect of grains and grain boundary resistance to the total resistance of NPs via studying the Cole–Cole plots, as shown in Fig. 10. It is observed that all the samples exhibit semi-circular arcs that are not complete, which are the result of the high resistance at low frequencies. Hence, the complete resistances of these are mostly equal to the grain boundary of the NPs. The behavior for BFO and excess samples could be explained by convolution in more than one semicircle, as shown in Fig. 11, where high-frequency semicircle represents the contribution of the grain and the low-frequency semicircle will represent the contribution of the grain boundary [11]. Further, the diameter of the semicircles corresponding to Bi-excess samples can be observed to be increased compared to that of BFO and found to be maximum for BFO5. This suggests that BFO5 NPs exhibit maximum grain resistance.

3.5 UV–vis spectroscopy

The energy bandgaps of BFO, BFO3, BFO5, BFO7, and BFO10 NPs have been analyzed by UV–vis absorption spectrum. The absorption spectrum of the
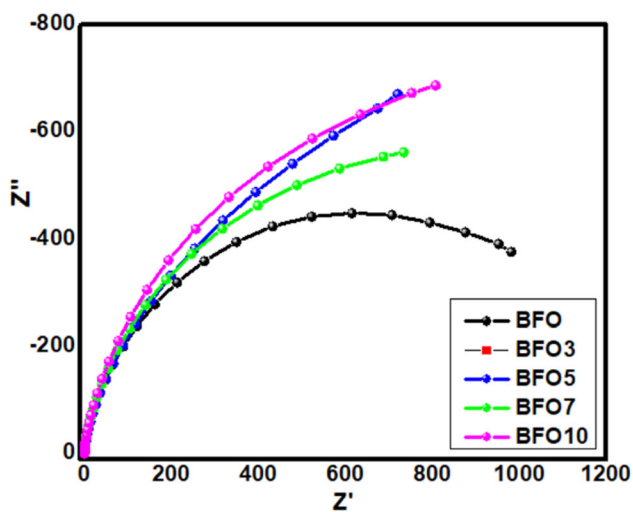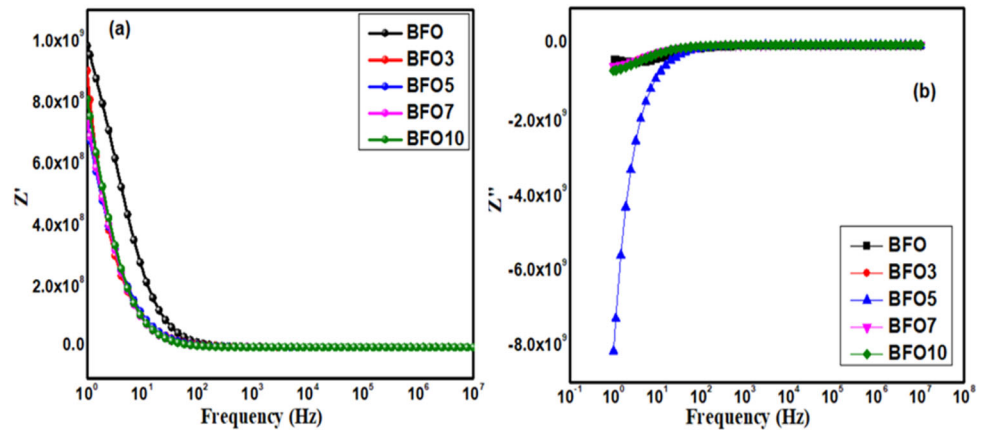
Fig. 10 Cole–Cole (Nyquist) plots for **a** BFO; **b** BFO3; **c** BFO5; **d** BFO7; **e** BFO10 NPs at room temperature

as-prepared BFO NPs in Fig. 12a–f. As demonstrated in the optical responses of BFO NPs, the absorption edges have been shifted towards the lower wavelength as the Bi-excess in BFO increases, indicating an increase in the bandgap energies. It was known that these bandgaps of BFO NPs would be calculated from the tangent line in the plots of the $(\alpha h\nu)^2$ vs. photon energy (hν), where the straight line intercepts on the x-axis. The direct bandgap energies are excerpted by using the formula: $(\alpha h\nu)^2 = \beta (h\nu - E_g)$, where hν is the absorbed photon energy; hν = 1240/λ (eV); α and β are absorption coefficients, respectively [29]. The values of direct bandgap energy obtained for BFO, BFO3, BFO5, BFO7, and BFO10 samples are displayed in Table 2. The increase in bandgap energies till BFO5 may be associated with the size differences and the change in P_{max} of synthesized BFO NPs. Beyond BFO5, the bandgap reduces

attributable to the enhanced Bi-excess content. These variations influence the local crystal fields and the undergoing electronic transitions leading to the modification in the absorption edges [13].

3.6 Magnetization

The response of Magnetization of BFO, BFO5, and BFO10 NPs with the applied magnetic field has been exhibited in Fig. 13a in the range ± 40,000 Oe. The plots demonstrate small hysteresis indicating the weak ferromagnetic behavior of the NPs. The nature of hysteresis near $H = 0$ can be observed in the range ± 1000 Oe in Fig. 13b. It is apparent from the curves that pure BFO shows a slight deviation from the normal hysteresis behavior by dwindling near $H = 0$. This pinch-off in the hysteresis indicates the spin exchange coupling interactions. The interactions between Bi^{3+} and Fe^{3+} may have been modulated in pure BFO (without Bi-excess) due to the fact that Bi evaporates due to its volatile nature and Bi:Fe ratio changes leading to the pinching off hysteresis. Gupta et al. have also reported such type of pinch-off in the hysteresis of $Pt/Bi_{1-x}Ce_xFeO_3/ITO$ thin films [30]. However, as the Bi-excess increases, the curve becomes normal, giving evidence for the regular alignment of the magnetic moments with the externally applied magnetic field. The values of maximum magnetization (M_{max}) and remnant magnetization (M_r) are displayed in Fig. 13c. The maximum value of M_{max} has been demonstrated by BFO5 of the magnitude 0.24 emu/g with the M_r of 0.2×10^{-2} emu/g. Likewise, the coercivity was also found to be minimum for the BFO5 sample. Even though the pure BFO shows significant M_{max} and M_r values, there exists a departure from the normal hysteresis
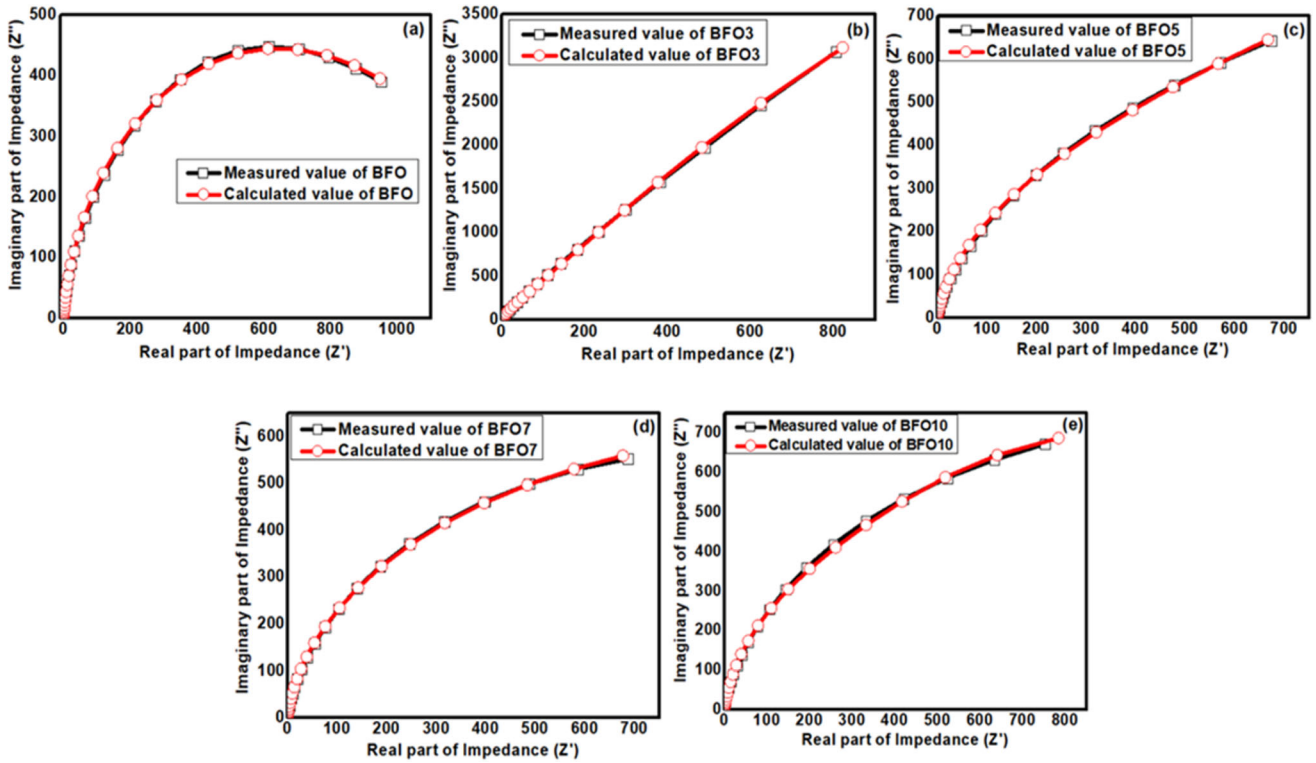
Fig. 11 Fitting of Cole–Cole plots for **a** BFO; **b** BFO3; **c** BFO5; **d** BFO7; **e** BFO10 NPs at room temperature
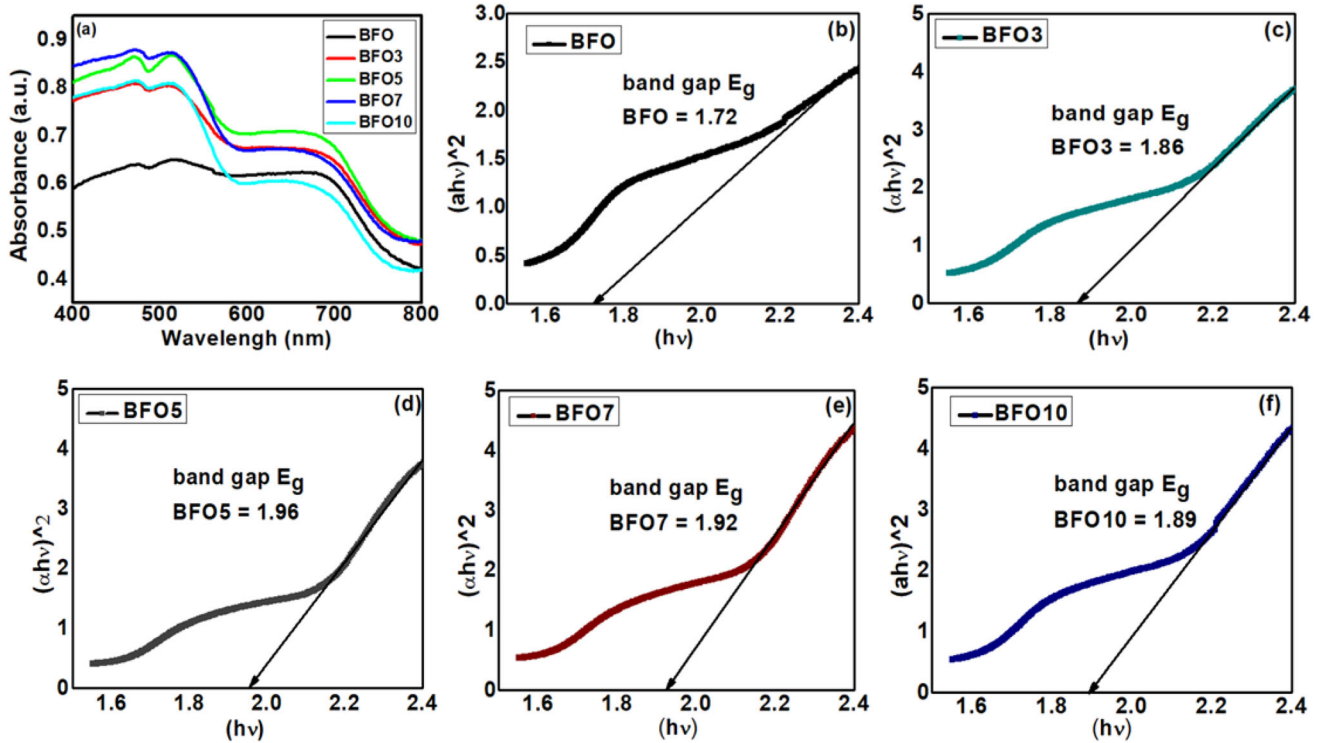
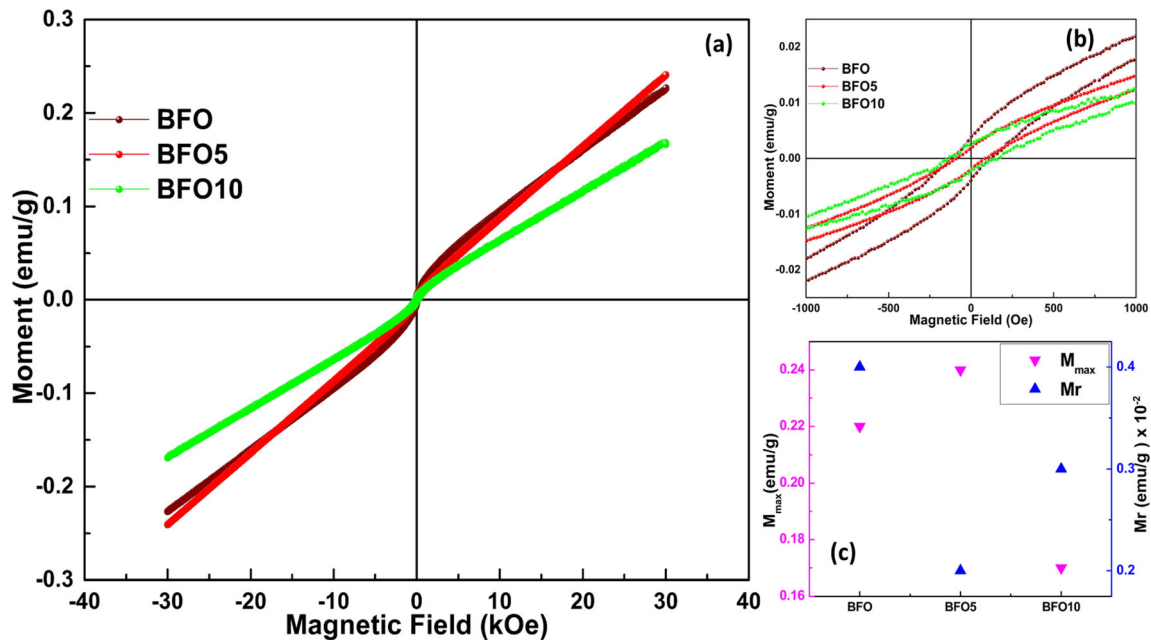**Fig. 12** UV–visible spectrum of **a** all samples; **b** BFO; **c** BFO3; **d** BFO5; **e** BFO7; **f** BFO10 NPs

Fig. 13 Magnetization curves for BFO; BFO5; BFO10 NPs **a** in the range ± 40,000 Oe; **b** in the range ± 1000 Oe; and **c** shows the values of M_{max} and M_r

behavior. The value of M_{max} increases for BFO5 and then decreases for BFO10. The enhancement in the magnetization can be associated with the size confinement effects of the NPs. As it has been observed in the structural analysis that the crystallite dimensions are minimum for BFO5, due to the size confinement, the spins uprise to the NP surfaces [31]. Therefore, despite being smaller spin densities, the BFO5 NPs produce noticeable magnetization.

Thus, the main reason responsible for the alteration of the properties of the Bi-excess $BiFeO_3$ nanoparticles with varying Bi content is that when the Bi content increases in the sample, it incorporates two modifications: one is that it provides excess electrons and enhance the electron density of the material; and second, it generates oxygen vacancies because the excess bismuth forms secondary phase. The enhanced oxygen vacancies in the interior and the accumulation of the space charge at the interfaces enhance the electrical, dielectric properties, and optical and magnetic properties up to 5% Bi-excess. Now, when the Bi-excess is increased beyond 5%, the electron density still increases but at the same time, the particle dimensions are decreasing, which hampers the movement of the electrons. This gives rise to the reduction of the polarization and dielectric constant along with the anomalous behavior of the

dielectric dispersion, ac conductivity, modulus, and impedance spectra.

4 Conclusions

A series of Bi-excess $BiFeO_3$ NPs were prepared by a sol–gel process in the present research work. The optimization of various properties such as structural, ferroelectric, electrical, optical, and magnetic properties was carried through different characterization techniques viz. X-ray diffraction (XRD) analysis, P–E loop measurements, dielectric constant, loss tangent (tan δ), AC conductivity (σ_{AC}), Modulus spectra analysis, Impedance analysis, Cole–Cole analysis of the impedance, UV–vis analysis, and magnetization. The successful employment of Bi-excess in BFO has been confirmed. The crystallite size and lattice parameters determined through XRD analysis were found to be minimum for BFO5 with a value of 41 nm and 8.78 Å, respectively. The strain has been found to be developed to 3.1×10^{-3} for BFO5 due to the reduced crystallite dimensions. The P–E loop measurements revealed the increasing maximum and remnant polarization for BFO5. Interestingly, the leakage current, examined by the P–E hysteresis loops, has been observed to be minimum for BFO5. The dielectric constant displayed decreasing

attributes with increasing frequency. BFO5 sample showed a high dielectric constant with smaller dielectric loss. The value of α which describes the dielectric relaxation was found to be in the range 0.7 ~ 0.9. The AC conductivity has been found to increase with increasing frequency. The impedance and modulus analysis revealed an excellent grain and grain boundary behavior in association with the internal resistances and capacitances of the NPs. The optical response of the NPs demonstrated an increasing bandgap with increasing Bi-excess, showing a maximum value of 1.96 eV for BFO5 NPs. The magnetization analysis confirmed the weak ferromagnetic behavior of the NPs with a maximum magnetization of 0.24 emu/g for BFO5 NPs. As a whole, the optimization of multiferroic properties of BFO NPs with Bi-excess has shown eminence for BFO5 NPs having 5% Bi-excess.

Acknowledgements

References

1. B. Kumari, P.R. Mandal, T.K. Nath, Magnetic, magnetocapacitance and dielectric properties of $BiFeO_3$ nanoceramics. Adv. Mater. Lett. **5**, 84–88 (2014). https://doi.org/10.5185/amlett.2013.fdm.36

2. T.H. Wang, C.S. Tu, H.Y. Chen, Y. Ding, T.C. Lin, Y.D. Yao, V.H. Schmidt, K.T. Wu, Magnetoelectric coupling and phase transition in BiFeO3 and (BiFeO3)0.95(BaTiO3)0.05 ceramics. J. Appl. Phys. **109**, 3–7 (2011). https://doi.org/10.1063/1.3551578

3. K. Javed, W.J. Li, S.S. Ali, D.W. Shi, U. Khan, S. Riaz, X.F. Han, Enhanced exchange bias and improved ferromagnetic properties in permalloy-BiFe0.95 Co0.05 O3 core-shell nanostructures. Sci. Rep. **5**, 1–9 (2015). https://doi.org/10.1038/srep18203

4. V.-A. Surdu, C. Roxana Doina Trus, S. Bogdan Vasile, O.C. Oprea, E. Tanas, L. Diamandescu, E. Andronescu, A.C. Ianculescu, Bi 1–x Eu x FeO 3 Powders: synthesis, characterization, magnetic and photoluminescence properties. Nanomaterials. **9**, 1–21 (2019). https://doi.org/10.3390/nano9101465

5. N. Zhang, D. Chen, F. Niu, S. Wang, L. Qin, Y. Huang, Enhanced visible-light photocatalytic activity of Gd-doped BiFeO3 nanoparticles and mechanism insight. Sci. Rep. **6**, 1–11 (2016). https://doi.org/10.1038/srep26467

6. T. Ito, T. Ushiyama, M. Aoki, Y. Tomioka, Y. Hakuta, H. Takashima, R. Wang, Oxygen diffusion and nonstoichiometry in BiFeO3. Inorg. Chem. **52**, 12806–12810 (2013). https://doi.org/10.1021/ic402069n

7. N. Miriyala, K. Prashanthi, T. Thundat, Oxygen vacancy dominant strong visible photoluminescence from $BiFeO_3$ nanotubes. Phys. Status Solidi - Rapid Res. Lett. **7**, 668–671 (2013). https://doi.org/10.1002/pssr.201308069

8. J. Wu, Z. Fan, D. Xiao, J. Zhu, J. Wang, Multiferroic bismuth ferrite-based materials for multifunctional applications: Ceramic bulks, thin films and nanostructures. Prog. Mater. Sci. **84**, 335–402 (2016). https://doi.org/10.1016/j.pmatsci.2016.09.001

9. M.Y. Shami, M.S. Awan, M. Anis-ur-rehman, Phase pure synthesis of $BiFeO_3$ nanopowders using diverse precursor via co-precipitation method. J. Alloys Compd. **509**, 10139–10144 (2011). https://doi.org/10.1016/j.jallcom.2011.08.063

10. S. Soni, S. Kumar, B. Dalela, S. Kumar, P.A. Alvi, S. Dalela, Defects and oxygen vacancies tailored structural and optical properties in CeO_2 nanoparticles doped with Sm3+ cation. J. Alloys Compd. **752**, 520–531 (2018). https://doi.org/10.1016/j.jallcom.2018.04.157

11. K. McDonnell, N. Wadnerkar, N.J. English, M. Rahman, D. Dowling, Photo-active and optical properties of bismuth ferrite ($BiFeO_3$): An experimental and theoretical study. Chem. Phys. Lett. **572**, 78–84 (2013). https://doi.org/10.1016/j.cplett.2013.04.024

12. R. Safi, H. Shokrollahi, Physics, chemistry and synthesis methods of nanostructured bismuth ferrite (BiFeO 3) as a ferroelectro-magnetic material. Prog. Solid State Chem. **40**, 6–15 (2012). https://doi.org/10.1016/j.progsolidstchem.2012.03.001

13. S. Li, Y.H. Lin, B.P. Zhang, Y. Wang, C.W. Nan, Controlled fabrication of BiFeO3 uniform microcrystals and their magnetic and photocatalytic behaviors. J. Phys. Chem. C. **114**, 2903–2908 (2010). https://doi.org/10.1021/jp910401u

14. P.C. Sati, M. Arora, S. Chauhan, M. Kumar, S. Chhoker, Structural, magnetic, vibrational and impedance properties of Pr and Ti codoped $BiFeO_3$ multiferroic ceramics. Ceram. Int. **40**, 7805–7816 (2014). https://doi.org/10.1016/j.ceramint.2013.12.124

15. A. Puhan, A.K. Nayak, B. Bhushan, S. Praharaj, S.S. Meena, D. Rout, Enhanced electrical, magnetic and optical behaviour of Cr doped Bi0.98Ho0.02FeO3 nanoparticles. J. Alloys Compd. **796**, 229–236 (2019). https://doi.org/10.1016/j.jallcom.2019.05.025

16. K. Kumari, R.N. Aljawfi, Y.S. Katharria, S. Dwivedi, K.H. Chae, R. Kumar, A. Alshoaibi, P.A. Alvi, S. Dalela, S. Kumar, Study the contribution of surface defects on the structural, electronic structural, magnetic, and photocatalyst properties of Fe: CeO2 nanoparticles. J. Electron Spectros. Relat. Phenomena. **235**, 29–39 (2019). https://doi.org/10.10 16/j.elspec.2019.06.004

17. A.M.M. Farea, S. Kumar, K.M. Batoo, A. Yousef, C.G. Lee, Alimuddin, Structure and electrical properties of Co0.5Cdx−Fe2.5−xO4 ferrites. J. Alloys Compd. **464**, 361–369 (2008). https://doi.org/10.1016/j.jallcom.2007.09.126

18. A.K. Sinha, B. Bhushan, A. Jagannath, R.K. Sharma, S. Sen, B.P. Mandal, S.S. Meena, P. Bhatt, C.L. Prajapat, A. Priyam, S.K. Mishra, S.C. Gadkari, Enhanced dielectric, magnetic and optical properties of Cr-doped BiFeO3 multiferroic nanoparticles synthesized by sol-gel route. Results Phys. **13**, 102299 (2019). https://doi.org/10.1016/j.rinp.2019.102299

19. M. Hashim, S. Alimuddin, S. Kumar, B.H. Ali, H. Koo, R. Chung, Kumar, Structural, magnetic and electrical properties of Al3+ substituted Ni-Zn ferrite nanoparticles. J. Alloys Compd. **511**, 107–114 (2012). https://doi.org/10.1016/j.jallc om.2011.08.096

20. A.S. Volkov, G.D. Koposov, R.O. Perfil'ev, A.V. Tyagunin, Analysis of experimental results by the Havriliak-Negami model in dielectric spectroscopy. Opt. Spectrosc. **124**, 202–205 (2018). https://doi.org/10.1134/S0030400X180 20200

21. J.J. Makosz, P. Urbanowicz, Relaxation and resonance absorption in dielectrics. Z. Für Naturforsch. A. **57**, 119–125 (2002). https://doi.org/10.1515/zna-2002-3-402

22. S. Kumar, Alimuddin, R. Kumar, P. Thakur, K.H. Chae, B. Angadi, W.K. Choi, Electrical transport, magnetic, and electronic structure studies of Mg0.95Mn0.05Fe2−2xTi2xO4±δ (0 <_ x <_ 0.5) ferrites. J. Phys. Condens. Matter. **19**, 476210 (2007). https://doi.org/10.1088/0953-8984/19/47/476210.

23. A.A. Kadam, S.S. Shinde, S.P. Yadav, P.S. Patil, K.Y. Rajpure, Structural, morphological, electrical and magnetic properties of Dy doped Ni–Co substitutional spinel ferrite. J. Magn. Magn. Mater. **329**, 59–64 (2013). https://doi.org/10. 1016/j.jmmm.2012.10.008

24. S. Kumari, N. Ortega, A. Kumar, S.P. Pavunny, J.W. Hubbard, C. Rinaldi, G. Srinivasan, J.F. Scott, R.S. Katiyar, Dielectric anomalies due to grain boundary conduction in chemically substituted BiFeO3. J. Appl. Phys. (2015). http s://doi.org/10.1063/1.4915110

25. M. Hashim, A. Alimuddin, S.E. Shirsath, S. Kumar, R. Kumar, A.S. Roy, J. Shah, R.K. Kotnala, Preparation and characterization chemistry of nanocrystalline Ni-Cu-Zn ferrite. J. Alloys Compd. **549**, 348–357 (2013). https://doi.org/ 10.1016/j.jallcom.2012.08.039

26. K.M. Batoo, S. Kumar, C.G. Lee, A. Alimuddinee, Finite size effect and influence of temperature on electrical properties of nanocrystalline Ni–Cd ferrites. Curr. Appl. Phys. **9**, 1072–1078 (2009). https://doi.org/10.1016/j.cap.2008.12.002

27. I. Coondoo, N. Panwar, M.A. Rafiq, V.S. Puli, M.N. Rafiq, R.S. Katiyar, Structural, dielectric and impedance spectroscopy studies in (Bi0.90R0.10)Fe0.95Sc0.05O3 [R = La, Nd] ceramics. Ceram. Int. **40**, 9895–9902 (2014). https://doi. org/10.1016/j.ceramint.2014.02.084

28. A. Selmi, S. Hcini, H. Rahmouni, A. Omri, M. Lamjed, A. Dhahri. Bouazizi, Synthesis, structural and complex impedance spectroscopy studies of Ni0.4Co0.4Mg0.2Fe2O4 spinel ferrite. Phase Transitions. **90**, 942–954 (2017). https://doi.org/ 10.1080/01411594.2017.1309403

29. J. Tauc, A. Menth, States in the gap. J. Non-Cryst. Solids. **10**, 569–585 (1972)

30. S. Gupta, M. Tomar, V. Gupta, Enhanced magnetic and electric properties of nanocrystalline Ce modified BFO thin films. Ferroelectrics **470**, 272–279 (2014). https://doi.org/10. 1080/00150193.2014.923735

31. A. Shokuhfar, S.S.S. Afghahi, Size controlled synthesis of FeCo alloy nanoparticles and study of the particle size and distribution effects on magnetic properties. Adv. Mater. Sci. Eng. (2014). https://doi.org/10.1155/2014/295390